Check for updates

Earth and Space Science

RESEARCH ARTICLE
10.1029/2025EA004631

Evaluating Multi-Agent and Wavelet-Transform Uncertainties in Lunar Seismic Ambient Noise Exploration

Kai Nierula[1], Sabrina Keil[2,3], Dmitriy Shutin[1], Ban-Sok Shin[1], and Heiner Igel[2]

[1]Institute of Communications and Navigation, German Aerospace Center (DLR), Wessling, Germany, [2]Ludwig-Maximilians-Universität München, Munich, Germany, [3]Geosciences Barcelona—CSIC, Barcelona, Spain

Key Points:

- Quantification of uncertainties in lunar ambient noise interferometry using multi-agent systems
- Uncertainty in Rayleigh wave velocities due to localization errors in multi-agent systems are acceptable, while timing errors are negligible
- Resolution limit of the continuous wavelet transform dominates error contribution in seismic Rayleigh wave velocity estimation

Correspondence to:
K. Nierula,
kai.nierula@dlr.de

Citation:
Nierula, K., Keil, S., Shutin, D., Shin, B.-S., & Igel, H. (2026). Evaluating multi-agent and wavelet-transform uncertainties in lunar seismic ambient noise exploration. *Earth and Space Science*, *13*, e2025EA004631. https://doi.org/10.1029/2025EA004631

Received 21 JUL 2025
Accepted 23 JAN 2026

Author Contributions:
Conceptualization: Kai Nierula, Dmitriy Shutin
Data curation: Sabrina Keil
Formal analysis: Kai Nierula
Funding acquisition: Ban-Sok Shin, Heiner Igel
Investigation: Kai Nierula
Methodology: Kai Nierula
Project administration: Dmitriy Shutin, Ban-Sok Shin, Heiner Igel
Software: Kai Nierula, Sabrina Keil
Supervision: Dmitriy Shutin, Heiner Igel
Validation: Kai Nierula
Visualization: Kai Nierula
Writing – original draft: Kai Nierula
Writing – review & editing: Dmitriy Shutin, Ban-Sok Shin

© 2026. The Author(s).
This is an open access article under the terms of the Creative Commons Attribution License, which permits use, distribution and reproduction in any medium, provided the original work is properly cited.

Abstract Passive seismic ambient noise interferometry (ANI) has shown potential for lunar seismic exploration, offering the capability to detect near-surface subsurface structures critical for future lunar mission, such as near-surface ice deposits and lava tubes, without the need for active seismic sources. Performing ANI on the Moon can be realized with a multi-agent system, in which a network of individual rovers either carry or deploy seismic receivers. However, these systems have inherent uncertainties in localization and timing. Additionally, methods used to extract dispersion curves from cross-correlations are fundamentally limited in achievable time–frequency resolution, which we demonstrate for the continuous wavelet transform (CWT). Quantifying how these factors propagate into Rayleigh wave velocity estimates is essential for accurate detection of lunar subsurface features. In this study, analytical error formulas are derived and validated through Monte Carlo simulations using passive seismic data from the Apollo 17 lunar seismic profiling experiment. Results indicate that velocity uncertainties due to localization errors remain around an acceptable 2.2 % for realistic positional standard deviations of 0.9 m at the receiver distance of 56.9 m as in the Apollo 17 Lunar Seismic Profiling Experiment. Timing errors induced by clock instabilities are negligible. However, uncertainties in seismic travel-time estimations are significantly dominated by the resolution limits imposed by the CWT. The developed analytical uncertainty model thus provides a critical foundation for designing autonomous lunar seismic networks for future lunar missions.

Plain Language Summary Exploring beneath the Moon's surface helps scientific research and supports future human missions. Detecting hidden ice or lava tubes can provide astronauts with resources and safe habitats. One way to investigate these hidden structures is through seismic methods, which study vibrations similar to those from earthquakes. Instead of waiting for moonquakes or artificially creating seismic signals, we can also measure natural vibrations occurring on the Moon. To measure lunar seismic signals, sensors must be placed on the surface. We propose using small rovers, called a multi-agent system, to carry or deploy these sensors. However, small errors in rover positioning and slight differences between their clocks might affect our measurements. To understand the impact of these uncertainties, we developed analytical formulas and validated them using data from the Apollo 17 mission. We found that positioning errors introduce only minor uncertainty, while clock differences have no impact. The main source of uncertainty actually comes from our analysis method, which inherently limits measurement precision. Overall, our findings confirm that multi-agent rover systems can support passive seismic exploration on the Moon. Our work helps improve rover networks and analysis techniques to detect hidden lunar subsurface features.

1. Introduction

1.1. Motivation

Driven by initiatives such as NASA's Artemis program, the Moon has reemerged as a prime target for scientific exploration and long-term human presence. Therefore, a central element of this initiative is identifying safe habitation sites and local resources. In particular, near-surface water-ice deposits in permanently shadowed regions near the lunar poles offer possibilities for in situ resource utilization (McClanahan et al., 2024; Reach et al., 2023). Extracting and processing lunar water could aid life support systems and provide essential components for rocket fuel (Spudis, 1999). Additionally, large underground cavities, particularly in the form of lava tubes, could serve as natural shelters for future astronauts by providing protection from cosmic radiation, micrometeorite impacts, and extreme temperature variations (Haruyama et al., 2012; Horz, 1985). However, the

direct detection of these structures remains challenging, with current evidence relying on collapsed pits and low-resolution orbital gravimetric measurements (Carrer et al., 2024; Chappaz et al., 2017).

Seismic exploration is a widely used technique to investigate subsurface structures on planetary bodies. It offers the capability of both detecting even small fractions of ice as well as cavities (Kolesnikov & Fedin, 2018; Kunimasu et al., 2023). Past lunar missions, such as the Apollo Passive Seismic Experiment, provided valuable insights, for example, into deep lunar structure and moonquake activity (Cooper et al., 1974). Several future lunar missions are planned or envisioned to bring back seismic stations to the Moon, for example, the Lunar Environment Monitoring Station for long-term seismic monitoring in the south polar region (Benna et al., 2020), the Farside Seismic Suite as a first station on the far side of the Moon (Panning et al., 2022), and the Lunar Geophysical Network spanning multiple locations around the Moon (Haviland et al., 2022). However, these concepts are meant for monitoring purposes. Despite the potential of seismic exploration, several challenges must be addressed. Unlike on Earth, where active seismic sources such as vibrators or explosives are commonly used (Talwani & Kessinger, 2003), deploying comparable sources on the Moon is far more difficult due to, for example, launch-mass, mechanical and operational constraints. The Moon's regolith, characterized by low seismic velocities and high scattering properties, further complicates seismic measurements by inducing wavefield coda and lowering waveform coherence, making it more difficult to process resulting seismic data (Blanchette-Guertin et al., 2015; Dainty et al., 1974). Additional challenges arise from the absence of an external positioning system, communication constraints due to the lack of a networking infrastructure, limited computational resources on lunar rovers and very high fluctuations in temperature of up to ≈ 300 K in equatorial regions (Saboia et al., 2024; Williams et al., 2017).

Concepts such as NASA's Cooperative Autonomous Distributed Exploration Rovers (de la Croix et al., 2024) aim to enhance planetary surface exploration by deploying autonomous, collaborative robotic networks. These so called multi-agent systems consist of multiple, usually homogeneous, agents with limited compute capabilities that perform collective exploration via inter-agent communication and local sensing of the environment (Şahin, 2005). They offer several advantages over single robots, for example, the ability to cover larger areas and provide redundancy (Schuster et al., 2020). Moreover, agents can self-localize, that is, determine their own position in (at least) a system-local coordinate system and distribute tasks (Brambilla et al., 2013).

To overcome the need for active seismic sources and the constraints of static and sparse single-station seismometer deployments, we propose using multi-agent systems equipped with seismometers to perform seismic ambient noise exploration for the mapping of water-ice deposits and lava tubes. In particular, seismic ambient noise interferometry (ANI) performed by a multi-agent system appears promising.

1.2. Main Contribution

As multi-agent systems have inherent uncertainties in localization and timing, seismic reconstruction results will be impacted. Additionally, the ANI processing workflow itself introduces uncertainties, most notably those associated with gathering the time-frequency information. We will demonstrate these for the continuous wavelet transform (CWT), though other more traditional methods such as the frequency-time analysis of seismic waves (FTAN) and the short-time Fourier transform (STFT) will have similar or worse behavior. Understanding these uncertainties will allow us to assess the feasibility of performing ANI with multi-agent networks for lunar seismic exploration. Additionally, these can be used in creating optimal experimental designs to reposition the agents for improved sensitivity for our specific goals (Strutz & Curtis, 2024).

Therefore, we use a combination of experimental data, analytical derivations, and simulations to analyze how localization and timing uncertainties inherent to autonomous rover networks propagate into ANI results and quantify the additional uncertainty introduced by the CWT. The notation used in this study is presented in Table 1.

In Section 2, we give an overview on the aspects of multi-agent systems that impact seismic measurements. In Section 3, we introduce the ideas behind ANI and how the time-frequency information is extracted via the CWT. In Section 4, we develop the analytical framework to derive the uncertainties related to the localization and timing errors, the CWT, and a combination of these. Section 5 details the origin and processing of the lunar data used for

23335084, 2026, 2, Downloaded from https://agupubs.onlinelibrary.wiley.com/doi/10.1029/2025EA004631 by Dtsch Zentrum F. Luft-U. Raum Fahrt In D. Helmholtz Gemein., Wiley Online Library on [24/02/2026]. See the Terms and Conditions (https://onlinelibrary.wiley.com/terms-and-conditions) on Wiley Online Library for rules of use; OA articles are governed by the applicable Creative Commons License

23335084, 2026, 2, Downloaded from https://agupubs.onlinelibrary.wiley.com/doi/10.1029/2025EA004631 by Dtsch Zentrum F. Luft-U. Raum Fahrt In D. Helmholtz Gemein., Wiley Online Library on [24/02/2026]. See the Terms and Conditions (https://onlinelibrary.wiley.com/terms-and-conditions) on Wiley Online Library for rules of use; OA articles are governed by the applicable Creative Commons License

Table 1
Notation Used in This Study

Symbol	Description
a	Scalar
$\boldsymbol{a}$	Vector
$\mathbf{A}$	Matrix
A	Random variable
$\mathbb{E}[A]$	Expectation of A
$\mathrm{Var}[A]$	Variance of A
$\boldsymbol{\Sigma}$	Covariance
$\mathcal{N}(\boldsymbol{a}, \boldsymbol{\Sigma})$	Normal distribution with mean $\boldsymbol{a}$ and covariance $\boldsymbol{\Sigma}$

our analysis. In Section 6, we show the setup of our uncertainty simulations. In Section 7, the results of these simulations is given and compared to our analytical ones. Section 8 concludes our work and gives an outlook on promising directions for future research.

2. Multi-Agent Systems

In the context of a seismic experiment, agents either place or carry seismic receivers. In the following, we therefore give a brief introduction on localization and timing in multi-agent systems and link these aspects to ANI. More details on how to assemble a multi-agent navigation system by integrating communication, localization, sensing, and control can be found in Zhang et al. (2021). The performance of their cooperative navigation in a space-analog environment is evaluated by Pöhlmann et al. (2023).

2.1. Localization in Multi-Agent Systems

Distance estimation via, for example, radio-frequency signals is the first step in localization. This is also referred to as ranging. The two-way time of arrival (TW-TOA) method allows for accurate ranging without requiring prior time synchronization between agents (Savic & Zazo, 2018). Afterward, the distance estimates are fused to get position estimates via a localization algorithm (Wymeersch et al., 2009).

For localization, the Cramér–Rao lower bound (CRB) establishes a theoretical lower limit on the error covariance matrix achievable by an unbiased position estimator (Cramér, 1946; Rao, 1992). It depends strongly on the signal propagation model, distance measurement type (e.g., TW-TOA), and the multi-agent system geometry (Ash & Moses, 2008). The accuracy bound corresponds to the covariance matrix from the CRB and can be visualized as uncertainty ellipses around position estimates (Chang & Sahai, 2006; Shen & Win, 2010). In practice, the mean square error in position estimation consists of both variance and bias, with bias often dominating in real-world scenarios (Conti et al., 2012).

In ANI, inter-receiver distances are essential to calculate velocities from the seismic wave traveltimes. However, rather than relying on RF-based ranging, distances should be derived from the localization algorithm's position estimates. This ensures the calculation of inter-receiver distances even when RF-based ranging is infeasible, for example, due to line-of-sight obstructions. Additionally, direct distance measurements only indicate how far receivers are apart, without providing information about the absolute measurement locations. Nevertheless, errors in the position estimates, which are fundamentally lower-bounded by the CRB discussed above, propagate into the inter-receiver distances and consequently affect the ANI results.

2.2. Timing in Multi-Agent Systems

Each agent carries a clock that relies on an oscillator whose frequency depends on the type of oscillator used (Levine, 1999). The frequency of any oscillator is unstable up to a certain degree due to inherent noise sources and can be impacted by environmental (e.g., thermal) variations (Sichitiu & Veerarittiphan, 2003). Therefore, synchronizing clocks is critical to enable coherent operation for localization, sensing, and communication tasks (Staudinger et al., 2021). In the context of ANI, clock instabilities among different receivers result in a non-uniform temporal reference for the recorded seismic traces, which impacts the cross-correlation of receivers' seismic traces.

The frequency stability of oscillators and clocks is often quantified using the overlapping Allan deviation (OADEV), defined as the square root of the two-sample variance of successive time differences over an averaging interval τ (Allan, 1966). It can be understood in a simplified manner as the average instability per second if the clock is observed over the interval τ. Figure 1 shows exemplary OADEVs for different clocks, with lower OADEVs generally indicating better performance. A region of low OADEV over τ indicates the most stable averaging interval. The averaging interval at which the OADEV begins to rise again after a minimum also determines the maximum synchronization interval to still be able to adequately estimate the clocks' states (Staudinger et al., 2021).

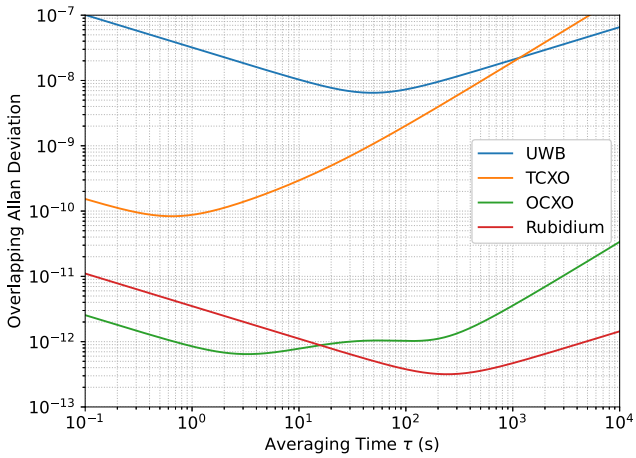

Figure 1. OADEVs for four different clock types. Data from Zhang et al. (2023) for the ultra-wideband clock, Staudinger et al. (2021) for the temperature controlled crystal oscillator (TCXO), and Trainotti et al. (2019) for the oven controlled quartz oscillator (OCXO) and Rubidum oscillator.

3. Ambient Noise Interferometry

ANI has been successfully applied in Earth-based seismology to image subsurface structures without the need for active sources (e.g., Lin et al., 2007; Yang et al., 2007). Similarly, for example, Larose et al. (2005), Tanimoto et al. (2008), and Sens-Schönfelder and Larose (2010) perform ANI with lunar data to investigate the local, near-surface subsurface, where thermal moonquakes act as the main seismic energy source (Duennebier & Sutton, 1974). Although ANI is predominantly used for monitoring, it has also been proposed for exploration applications as well (Ma et al., 2024). Recent advancements, such as improved stacking methods, significantly reduce measurement times and enhance ANI's potential for planetary exploration (Keil et al., 2024).

ANI is based on the principle that cross-correlations of diffuse wavefields approximate the empirical Green's function between two receivers, that is, the Green's function of a propagation model between them (Lobkis & Weaver, 2001) (Figures 2a–2c). In the seismic applications, ambient seismic noise can act as the diffuse wavefield, provided it is coherent and propagates through both receivers. As a result, one receiver effectively acts as a virtual source, while the other records the seismic response as if the first station had

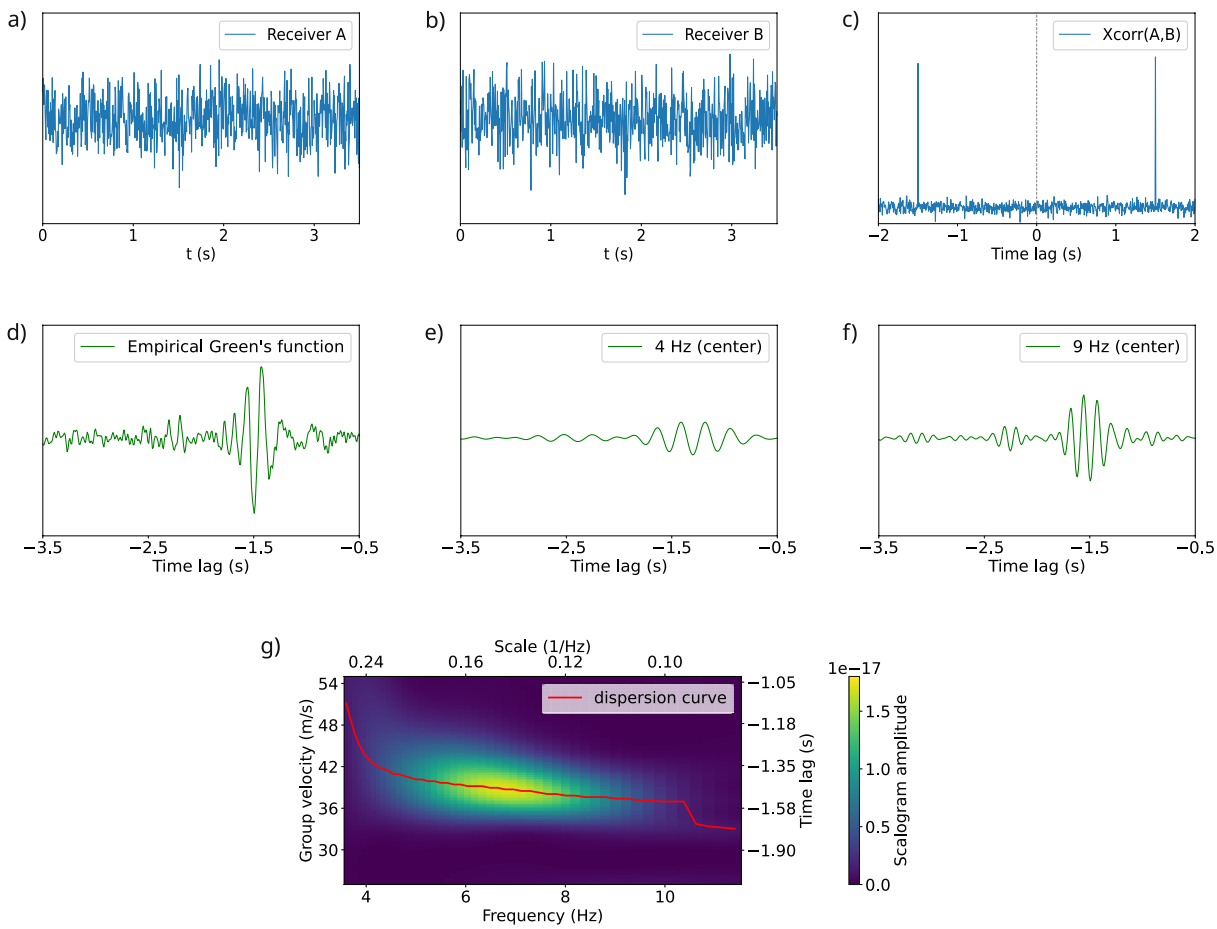

Figure 2. Main concept of ambient noise interferometry and processing steps. The cross-correlation of simulated isotropic, uncorrelated noise fields measured at receivers A and B as shown in (a) and (b) results in the emergence of Green's function (c). (d) Shows the empirical Green's function for the cross-correlation of measured Apollo 17 lunar data and its frequency-dependency in (e) and (f). (g) Depicts a scalogram and the dispersion curve derived using the continuous wavelet transform of the Green's function from (d).

23335084, 2026, 2, Downloaded from https://agupubs.onlinelibrary.wiley.com/doi/10.1029/2025EA004631 by Dtsch Zentrum F. Luft-U. Raum Fahrt In D. Helmholtz Gemein., Wiley Online Library on [24/02/2026]. See the Terms and Conditions (https://onlinelibrary.wiley.com/terms-and-conditions) on Wiley Online Library for rules of use; OA articles are governed by the applicable Creative Commons License

23335084, 2026, 2, Downloaded from https://agupubs.onlinelibrary.wiley.com/doi/10.1029/2025EA004631 by Dtsch Zentrum F. Luft-U. Raum Fahrt In D. Helmholtz Gemein., Wiley Online Library on [24/02/2026]. See the Terms and Conditions (https://onlinelibrary.wiley.com/terms-and-conditions) on Wiley Online Library for rules of use; OA articles are governed by the applicable Creative Commons License

emitted an impulsive signal (Sabra et al., 2005). Surface waves, for example, Rayleigh waves, dominate the Green's function and therefore are the easiest to extract from ambient noise (Shapiro & Campillo, 2004). These are inherently dispersive, meaning that velocity varies with frequency in non-homogeneous media, as lower frequencies are sensitive to deeper structures compared to higher-frequency waves (Lin et al., 2007) (Figures 2d–2f).

To determine frequency-dependent velocities, frequency-dependent traveltimes between the virtual source and receiver need to be extracted. As these traveltimes correspond to frequency-dependent lag times of Green's function, time-frequency or time-scale analysis methods are typically used (Bensen et al., 2007). More traditional time-frequency methods (e.g., FTAN and STFT), face limitations, for example, due to their fixed resolution in time-frequency space. In contrast, the CWT that we employ in this research offers adaptive resolution, improving the trade-off between frequency and temporal resolution (Mallat, 2009; Torrence & Compo, 1998). The CWT has been used in multiple studies related to extracting the velocity of surface waves, for example, Kulesh et al. (2005); Holschneider et al. (2005); Poggi et al. (2013); Gupta and Mukhopadhyay (2023). It convolves the signal $f(t)$ with the complex conjugate of a dilated and translated mother wavelet $\psi(t)$. The squared modulus of this convolution is called scalogram and depicts the energy that specific scales (which are inversely proportional to frequency) have at certain times (see Appendix A for details on the CWT) (Figure 2g)). Practically, dispersion curves are extracted directly from the scalogram by identifying per-scale maxima. Compared to FTAN and STFT, the CWTs resolution of the energy is superior (Cohen, 2001). The dispersion curves correspond to the empirical Green's function, that is, the frequency-dependent traveltimes of the seismic wave (Kulesh et al., 2008). Inter-station surface-wave velocities are then calculated using the picked traveltimes from the scalogram and the distances between station pairs (Figure 2g)).

In the context of lunar seismic exploration, Keil et al. (2024) numerically investigated the potential of ANI in the highly scattering lunar environment. Their results show that inter-receiver distances of up to approximately 60, m are usable within the frequency range of thermal moonquakes. Beyond this distance, a reduction in signal-to-noise ratio (SNR) obscures the emergence of the empirical Green's function. We consider this spacing sufficient for exploratory measurements, while also facilitating inter-receiver communication (Staudinger et al., 2023).

4. Methodology

This section (a) develops closed-form expressions that map multi-agent localization uncertainties and wavelet-based time-lag, that is, travel time, picking errors to the mean and variance of inter-receiver velocity estimates derived with ANI, and (b) describes a model for ultra-wideband (UWB) clocks that is later used in simulations to assess the impact of clock instabilities on the velocity reconstruction.

4.1. Localization-Error-Induced Distance Uncertainty

The position of an agents is a random quantity due to errors in the localization method (Section 2.1). Let X_1 and X_2 be receiver positions in $\mathbb{R}^2$ that are carried or placed by agents and therefore have position errors. We quantify the position estimates as independent, circular-symmetric bivariate normal distributions

$$X_1 \sim \mathcal{N}(\boldsymbol{\mu}_1, \boldsymbol{\Sigma}_1), \qquad X_2 \sim \mathcal{N}(\boldsymbol{\mu}_2, \boldsymbol{\Sigma}_2), \tag{1}$$

centered on $\boldsymbol{\mu}_1$ and $\boldsymbol{\mu}_2$ with covariance matrices $\boldsymbol{\Sigma}_1 = \boldsymbol{\Sigma}_2 = \sigma_p^2 \mathbf{I}_2$, where σ_p is the equal, component-wise standard deviation of the position estimates (Figure 3).

The inter-receiver distance L can be be computed as

$$L = \|\Delta X\| = \|X_1 - X_2\|. \tag{2}$$

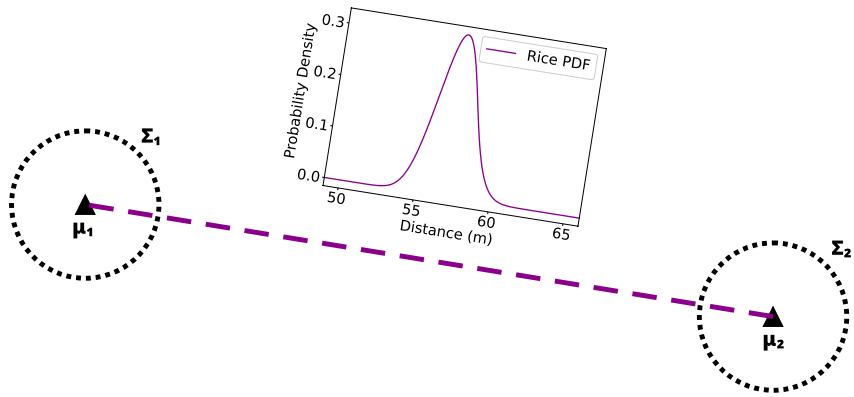

Figure 3. Two unknown receiver positions with independent, circular-symmetric bivariate normal distributions $\mathcal{N}(\boldsymbol{\mu}, \boldsymbol{\Sigma})$ and the resulting Rice distribution for the distance estimate.

L is known to be Rice-distributed (Rice, 1945) with the probability density function

$$f_D(\ell|\nu,\alpha) = \frac{\ell}{\alpha^2}\exp\left(-\frac{(\ell^2+\nu^2)}{2\alpha^2}\right) I_0\left(\frac{\ell\nu}{\alpha^2}\right), \tag{3}$$

scale $\alpha = \sqrt{2}\sigma_p$ and non-centrality $\nu = \|\boldsymbol{\mu}_1 - \boldsymbol{\mu}_2\|$. Its mean is given as

$$\mathbb{E}[L] = \alpha\sqrt{\frac{\pi}{2}} L_{1/2}\left(\frac{\nu^2}{2\alpha^2}\right) = \alpha\sqrt{\frac{\pi}{2}} e^{x/2}\left[I_0\left(-\frac{\nu^2}{2\alpha^2}\right) + I_1\left(-\frac{\nu^2}{2\alpha^2}\right)\right], \tag{4}$$

where $L_{1/2}$ denotes the Laguerre polynomial (Half) and I_0, I_1 are modified Bessel functions of first kind. The variance can then be computed as

$$\mathrm{Var}[L] = 2\alpha^2 + \nu^2 - \mathbb{E}[L]^2. \tag{5}$$

It follows that the mean and variance of the wave velocity estimates V can then be calculated as

$$\mathbb{E}[V] = \frac{\mathbb{E}[L]}{t}, \qquad \mathrm{Var}[V] = \frac{\mathrm{Var}[L]}{t^2}, \tag{6}$$

where t is a deterministic time lag.

4.2. Clock-Instability-Induced Time-Lag Uncertainty

In the derivation above, we assumed that the time lag t is deterministic. This assumption might be too strong, as the time lag t results from the cross-correlation of two seismic traces recorded by different agents with clock instabilities.

To inspect the impact that clock instability has on the retrieval of the Green's function, we inspect UWB clocks as a conservative, "worst-case" scenario, and due to the benefits of UWB devices in real-world scenarios: being cheap and providing communication and ranging capabilities. We employ the two-state clock model with constant frequency drift d from Galleani et al. (2003) to simulate the clocks. An iterative solution with constant time spacing $\Delta t = t_{i+1} - t_i$ for the state $\mathbf{x} = [x_1, x_2]^\top$ that stacks the clock phase and frequency errors can be derived by calculating

23335084, 2026, 2, Downloaded from https://agupubs.onlinelibrary.wiley.com/doi/10.1029/2025EA004631 by Dtsch Zentrum F. Luft-U. Raum Fahrt In D. Helmholtz Gemein., Wiley Online Library on [24/02/2026]. See the Terms and Conditions (https://onlinelibrary.wiley.com/terms-and-conditions) on Wiley Online Library for rules of use; OA articles are governed by the applicable Creative Commons License

$$\mathbf{x}_{k+1} = \begin{bmatrix} 1 & \Delta t \\ 0 & 1 \end{bmatrix} \mathbf{x}_k + \begin{bmatrix} \frac{1}{2}\Delta t^2 \\ \Delta t \end{bmatrix} d + \mathbf{w}_k\,, \qquad \mathbf{w}_k \sim \mathcal{N}\left(\mathbf{0}, \begin{bmatrix} \sigma_w^2\,\Delta t + \sigma_r^2\,\frac{\Delta t^3}{3} & \sigma_r^2\,\frac{\Delta t^2}{2} \\ \sigma_r^2\,\frac{\Delta t^2}{2} & \sigma_r^2\,\Delta t \end{bmatrix}\right), \tag{7}$$

where σ_w^2, σ_r^2 are the variances of the white and random-walk frequency noise components, respectively.

4.3. CWT-Induced Time-Lag Uncertainty

Let us now consider a theoretical case where the receiver positions are known, therefore the distance ℓ is now deterministic. When using the CWT to extract time-frequency information from the empirical Green's function (Figure 2), the joint time-frequency resolution of the scalogram is limited due to the Heisenberg-Gabor uncertainty principle (Mallat, 2009). Here, we quantify the impact of this resolution limit on the accuracy of the time-lag pick t as the per-frequency maximum of the scalogram.

The limited joint time-frequency resolution can be understood as energy spreading around a point in the scalogram. For our purpose, we will only consider the spread in time. In our work we employ the Morlet wavelet

$$\psi(t) = \pi^{-1/4} e^{i\omega_0 t} e^{-t^2/2} \tag{8}$$

as mother wavelet $\psi(t)$ centered at 0, where ω_0 is the dimensionless central frequency of the Gaussian-windowed sinusoid and a trade-off parameter between time and frequency resolution. Its energy spread in time is

$$\sigma_{E,t} = s\sigma_t\,, \tag{9}$$

with scale s and time variance

$$\sigma_t = \frac{1}{\sqrt{2}} \tag{10}$$

(derivation in Appendix A).

From Equation 9, we see that the energy is spread across a larger time interval with increasing scale s, that is, lower wave frequencies. We model the uncertainty in time-lag pick in the scalogram as normal distributions with the mean $\mu_{E,t}$ being the maximum picks, that is, the unmodified dispersion curve, and the standard deviations $\sigma_{E,t} = s/\sqrt{2}$. Since we now treat the time lag T as a random variable, its appearance in the denominator of $V = \ell/T$ could result in singular inverse moments $\mathbb{E}\left[T^{-1}\right]$ and $\mathrm{Var}\left[T^{-1}\right]$. By truncating the normal distribution $T \sim \mathcal{N}\left(\mu_{E,t}, \sigma_{E,t}\right)$ at a lower truncation point a, we can approximate $\mathbb{E}\left[T^{-1}\right]$ and $\mathrm{Var}\left[T^{-1}\right]$ using Dawson's integral as in Hall (1979). This approximation holds as long as

$$\left(\frac{\sigma_{E,t}}{\mu_{E,t}}\right)^2 \leq \frac{a}{\mu_{E,t}} \leq \frac{1}{25}. \tag{11}$$

The mean and variance of the inverse truncated normal distribution can then be approximated by

$$\mathbb{E}\left[T^{-1}\right] \approx \frac{I(\sigma_1)}{\mu_{E,t}}, \qquad \mathrm{Var}\left[T^{-1}\right] \approx \frac{J(\sigma_1) - I^2(\sigma_1)}{\mu_{E,t}^2}, \tag{12}$$

where $\sigma_1 = \sigma_{E,t}/\mu_{E,t}$, and I and J are derived using Dawson's integral D as such:

$$D(x) = e^{-x^2} \int_0^x e^{t^2}\,dt\,, \qquad I(\sigma_w) = \frac{\sqrt{2}}{\sigma_w} D\left(\frac{1}{\sqrt{2}\,\sigma_w}\right), \qquad J(\sigma_w) = \frac{1}{\sigma_w^2}[I(\sigma_w) - 1]. \tag{13}$$

23335084, 2026, 2, Downloaded from https://agupubs.onlinelibrary.wiley.com/doi/10.1029/2025EA004631 by Dtsch Zentrum F. Luft-U. Raum Fahrt In D. Helmholtz Gemein., Wiley Online Library on [24/02/2026]. See the Terms and Conditions (https://onlinelibrary.wiley.com/terms-and-conditions) on Wiley Online Library for rules of use; OA articles are governed by the applicable Creative Commons License

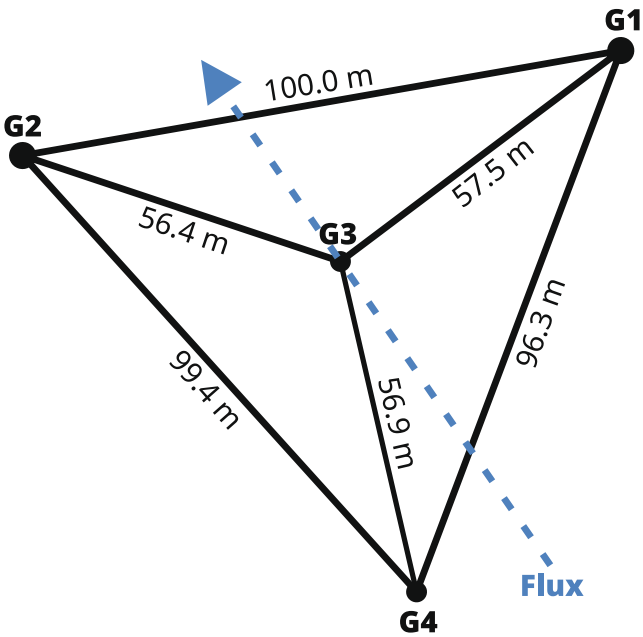

Figure 4. Array geometry of the Apollo 17 lunar seismic profiling experiment, with inter-station distances from Haase et al. (2019) and noise flux direction from Larose et al. (2005).

With the distance ℓ being deterministic, moments of V then follow as

$$\mathbb{E}[V] = \ell\mathbb{E}\left[T^{-1}\right], \qquad \mathrm{Var}[V] = \ell^2\mathrm{Var}\left[T^{-1}\right]. \tag{14}$$

4.4. Combined Uncertainties

With both L and T treated as random variables, V follows as the ratio of these two random variables: $V = L/T$. Instead of calculating the distribution of V, we focus solely on the mean and variance of V, as these are easier to derive. As we will see later, we can neglect the impact of the clock instabilities (Sec. 7), and therefore only have to account for the moments stemming from the Rice distribution for L and the inverse truncated normal distribution for T^{-1}.

Assuming that the random variables L and T^{-1} are independent, the mean and variance of V can be exactly computed (Goodman, 1960) as

$$\begin{aligned}\mathbb{E}[V] &= \mathbb{E}[L]\,\mathbb{E}\left[T^{-1}\right]\\ \mathrm{Var}[V] &= \left(\mathrm{Var}[L] + \mathbb{E}[L]^2\right)\left(\mathrm{Var}\left[T^{-1}\right] + \mathbb{E}\left[T^{-1}\right]^2\right) - \left(\mathbb{E}[L]\mathbb{E}\left[T^{-1}\right]\right)^2\end{aligned} \tag{15}$$

As this is a strong assumption, we will test if it holds in Section 7. Without the assumption of independence of L and T^{-1}, calculating these moments can be done using a first-order Taylor series approximation around $\boldsymbol{\theta} = \left(\mathbb{E}[L], \mathbb{E}\left[T^{-1}\right]\right)$ (Stuart & Ord, 1994), resulting in

$$\begin{aligned}\mathbb{E}[V] &\approx \mathbb{E}[L]\mathbb{E}\left[T^{-1}\right]\\ \mathrm{Var}[V] &\approx \mathbb{E}[L]^2\mathrm{Var}[L] + \mathbb{E}[L]^2\mathrm{Var}\left[T^{-1}\right] + 2\mathbb{E}[L]\mathbb{E}\left[T^{-1}\right]\mathrm{Cov}\left[L, T^{-1}\right]\end{aligned} \tag{16}$$

with the covariance term $\mathrm{Cov}\left[L, T^{-1}\right]$.

5. Apollo 17 Lunar Seismic Profiling Experiment Data and Processing

We apply our approach to data from the Apollo 17 Lunar Seismic Profiling Experiment (LSPE) (Kovach et al., 1973) which serve as the basis for our simulations described in Section 6. Four seismic receivers were deployed in a triangular configuration with a central station (Figure 4, labeled G1–G4). Inter-station distances are taken from Haase et al. (2019), who corrected the original distances by combining new high-resolution data from the Lunar Reconnaissance Orbiter with Apollo astronaut photography. The receivers recorded vertical ground velocity in a usable frequency range of 3–30 Hz with a sampling rate of 118 Hz. For more details on instruments and recording formats, see, for example Kovach et al. (1973). While the LSPE was primarily set up as an active source experiment, passive data were also recorded, in particular continuously between 15 August 1976 and 24 April 1977.

For our purpose we used 1 month (19 September–19 October 1976) of passive data from Data ARchives and Transmission System (DARTS) (see Data Availability Statement) in decoded CSV format. This has been shown to be a long enough period for the empirical Green's function to converge to the one that would appear if all 8 months of data were used, thereby reducing the computational effort (Keil et al., 2024). We focus on station pair G3–G4 only, as it has shown to have the highest SNR of the station pairs due to the relatively short inter-station distance and the closest match of incident direction of the principal seismic noise sources with the G3–G4 setup (Larose et al., 2005; Tanimoto et al., 2008) (Figure 4).

The raw data were filtered in the frequency range 3 Hz to 30 Hz, the signal's amplitude capped to three times the root mean square of the raw data, and spectrally whitened. Afterward, the seismic traces between G3–G4 were

23335084, 2026, 2, Downloaded from https://agupubs.onlinelibrary.wiley.com/doi/10.1029/2025EA004631 by Dtsch Zentrum F. Luft-U. Raum Fahrt In D. Helmholtz Gemein., Wiley Online Library on [24/02/2026]. See the Terms and Conditions (https://onlinelibrary.wiley.com/terms-and-conditions) on Wiley Online Library for rules of use; OA articles are governed by the applicable Creative Commons License

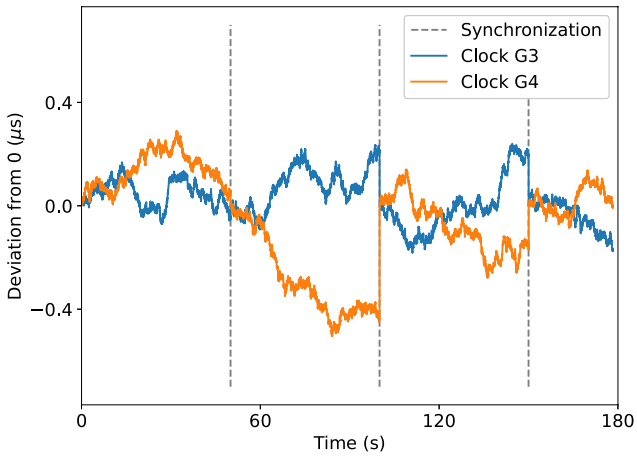

Figure 5. Simulation of the two ultra-wideband clocks that perfectly synchronize every 50 s.

correlated using the python package MSNoise (Lecocq et al., 2014) for 30 min time windows and linearly stacked. Subsequently, the CWT was used to locate the per-frequency-maxima of the correlated signal in the same frequency range of 3.6 Hz to 11.4 Hz as in Larose et al. (2005) and Sens-Schönfelder and Larose (2010).

6. Simulation Setup

We perform different simulations to quantify how the different uncertainty factors impact the velocity results and to confirm the analytical derivations from Section 4. All of these will rely on the Apollo 17 LSPE data from Section 5, either by making use of the time lags from the scalogram or by modifying the seismic traces directly in case of the clock-instability-induced uncertainties.

First, we simulate the impact of localization uncertainty only, neglecting other uncertainties. To this end, we assume $\sigma_p = 0.9$ m, which corresponds to the maximum root-mean-square error (RMSE) of two agents in the vicinity of anchors as observed in experiments by Pöhlmann et al. (2023). The Euclidean distance is then calculated between 100 000 random receiver positions X_1 and X_2 sampled from the normal distributions as defined in Equation 1, with means being the original G3 and G4 positions, respectively. The per-scale velocity estimate is then calculated by dividing the distance samples with time lags picked from the scalogram.

Second, 1,000 realizations of two UWB clocks are created using Equation 7 with clock parameters $\sigma_w^2 = 1.02 \cdot 10^{-15}$ s, $\sigma_r^2 = 1.29 \cdot 10^{-18}$ Hz and $d = 1.47 \cdot 10^{-22}$ Hz (Figure 6). dt is set to be equal to the sampling period of the original seismometers to allow for easy addition of the simulated instability to the original timestamps. We perfectly synchronize the clocks every 50 s (minimum of the OADEV in Figure 1) by resetting the clock phase and frequency errors to $[0,0]^T$ (Equation 7). Two exemplary clock instability simulations with synchronization are shown in Figure 5. We then shift the timestamps of the seismic traces of G3 and G4 by the simulated deviation. To correlate the two seismic traces, we linearly interpolate the data back to the original timestamps. The modified seismic traces are then processed as the original ones were (Section 5) and the dispersion curve is extracted.

Third, to ascertain the effect of solely uncertainties in the time lag t due to the energy spread of the CWT, we generate 100 000 time-lag samples T from the truncated normal distribution $\mathcal{N}(\mu_{E,t}, \sigma_{E,t})$ per scale s. A truncation point of $a = 0.055$ s ((11)) was selected to approximate the moments of the inverse truncated normal distribution for the time lag, following a manual optimization. The dispersion curve then follows from $V = \ell/T$ with $\ell = 56.9$ m between G3 and G4.

Fourth, to simulate a combination of uncertainty in position and time we take one distance L and one time-lag sample T per scale to calculate a single dispersion curve. We repeat this 100 000 times to get the moments of our velocity estimates (Equation 15). We also check if the assumption on the independence of L and T^{-1} holds by numerically estimating the covariance $\mathrm{Cov}[L, T^{-1}]$ and calculating the impact of dropping the covariance term in the Taylor approximation of $\mathrm{Var}[V]$ (Equation 16). Additionally, the difference between the Taylor approximation and the exact formulation (Equation 15) is calculated.

An overview of the simulation parameters is presented in Table 2. We also assess the impact of different w_0 parameters of the Morlet wavelet (Equation 8) by repeating all simulations. Based on these repetitions, we compare the analytically derived and simulated mean and standard deviation of the velocity estimates V in case of the combined uncertainty factors.

7. Results and Discussion

In this section, we will first go over the results from the simulations before confirming that our analytical derivations match the moments from the simulations. Please note that the standard deviations shown will stem from

23335084, 2026, 2, Downloaded from https://agupubs.onlinelibrary.wiley.com/doi/10.1029/2025EA004631 by Dtsch Zentrum F. Luft-U. Raum Fahrt In D. Helmholtz Gemein., Wiley Online Library on [24/02/2026]. See the Terms and Conditions (https://onlinelibrary.wiley.com/terms-and-conditions) on Wiley Online Library for rules of use; OA articles are governed by the applicable Creative Commons License

23335084, 2026, 2, Downloaded from https://agupubs.onlinelibrary.wiley.com/doi/10.1029/2025EA004631 by Dtsch Zentrum F. Luft-U. Raum Fahrt In D. Helmholtz Gemein., Wiley Online Library on [24/02/2026]. See the Terms and Conditions (https://onlinelibrary.wiley.com/terms-and-conditions) on Wiley Online Library for rules of use; OA articles are governed by the applicable Creative Commons License

Table 2
Simulation Parameters for the Different Scenarios

Uncertainty source	Parameter	Symbol	Value/Setting
Localization	Std of position error	σ_p	0.9 m
	Receiver means	$\boldsymbol{\mu}_1, \boldsymbol{\mu}_2$	G3 and G4 coordinates
	Covariance matrix	$\boldsymbol{\Sigma}_1 = \boldsymbol{\Sigma}_2$	$\sigma_p^2 \mathbf{I}_2$
	No. samples		100 000 receiver pairs
Clock instability	White noise variance	σ_w^2	$1.02 \cdot 10^{-15}$ s
	Random walk variance	σ_r^2	$1.29 \cdot 10^{-18}$ Hz
	Drift component	d	$1.47 \cdot 10^{-22}$ Hz
	Time step	Δt	$8.49 \cdot 10^{-3}$ s
	Sync. interval		50 s
	No. samples		1,000 clock pairs
CWT	Inter-receiver distance	ℓ	56.9 m
	Mean of time-lag	$\mu_{E,t}$	Max. pick in scalogram p. scale
	Std of time-lag	$\sigma_{E,t}$	$s/\sqrt{2}$
	No. samples		100 000 p. scale
Combined	Distance sample	L	From localization
	Time-lag sample	T	From CWT
	No. samples		1 p. scale for 100 000 rec. pairs

different kinds of distributions, for example, a scaled Rice distribution the velocity estimates in case of only localization errors.

Figure 6 shows the scalograms and picked dispersion curves for different ω_0s of the Morlet wavelet. The main energy is concentrated between approximately 6 Hz to 8 Hz and how concentrated it is depends strongly on the choice of ω_0. Additionally, small differences between the dispersion curves are noticeable for the different ω_0s at lower and higher frequencies. For $\omega_0 = 6$, the dispersion curve mostly follows the one for $\omega_0 = 8$, with the exception of around 10 Hz, where the maximum energy is similar to the $\omega_0 = 4$-case. For $\omega_0 = 6$, the dispersion curve then jumps to another band of slightly higher energy, where it is again more similar to the $\omega_0 = 8$-case. As we are more concerned with uncertainties than the exact shape of the dispersion curves, we only note here that an amplitude-scaled scalogram for the ridge detection might be a better choice to pick the dispersion curves (see Appendix A).

7.1. Localization-Error-Induced Distance Uncertainty

With the assumed σ_p of 0.9 m, the standard deviation in distance estimate comes to $\sqrt{\mathrm{Var}[L]} \approx 1.27$ m (Equation 5). The final standard deviations in the velocity estimates come from scaling with the time lags (Equation 6),

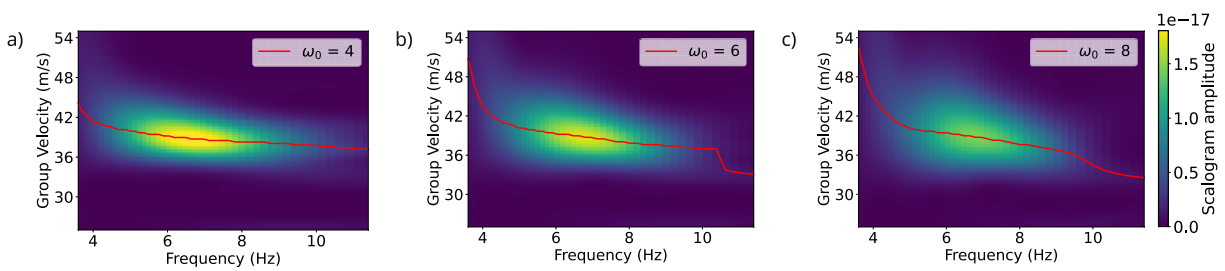

Figure 6. Scalograms for (a) $\omega_0 = 4$, (b) $\omega_0 = 6$, and (c) $\omega_0 = 8$ with already converted axes (scale to frequency and time to velocity). The dispersion curves are depicted in red.

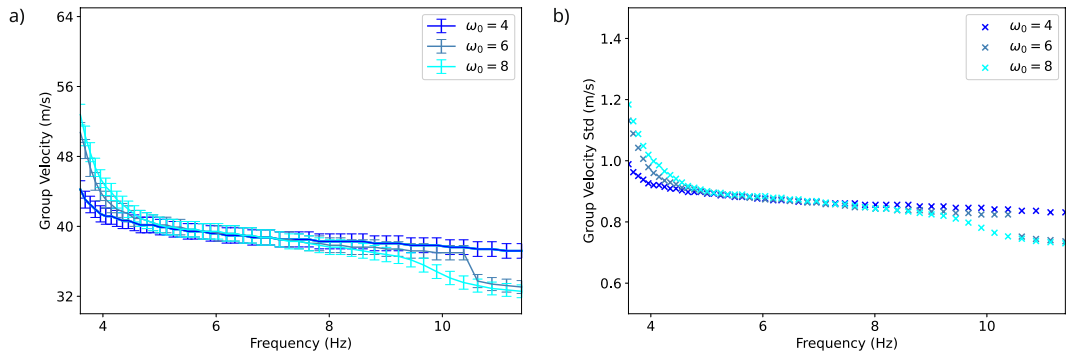

Figure 7. Dispersion curves for different ω_0s with standard deviation of the velocity estimates solely due to uncertainty in localization (a) and closer look at the standard deviations (b).

which change with frequency and choice of ω_0. Therefore, the standard deviations mimic the shape of the dispersion curve (Figure 7). The standard deviations are $\approx 2\,\%$ of the mean velocity, indicating that the impact from positional errors induced by the multi-agent localization method on the velocity reconstruction are only minor. Nonetheless, this analysis assumed identical, circular-symmetric Gaussian position errors for both receivers. More realistic shapes of the position error distributions, for example, inspired by the elliptical CRB with agent-specific covariance matrices would most likely alter the variance in the distance estimate. Additionally, the RMSE in position estimates of 0.9 m was only the maximum in a specific network configuration and would change in other scenarios.

7.2. Clock-Instability-Induced Time-Lag Uncertainty

Next, we evaluate the impact of the clock instabilities with $\omega_0 = 8$, as it has shown the highest velocities (Figure 7). Naturally, we would expect that the higher the velocity of the seismic wave is, the more accurate the clocks have to be to capture this dynamic. In Figure 8, we see that the dispersion curves from the 1,000 simulations overlap for all simulations. There is a clear difference between these 1,000 dispersion curves and the one derived with the original, unmodified data. This difference most likely occurs because we interpolated the small shifts in the timestamps of the seismic data back onto the original time grid. Here, we allow non-integer amplitude values. These no longer match the original integer amplitudes, and these changes propagate into the dispersion analysis. As there is no difference between the 1,000 clock simulations, we can still deduce that clock instabilities present in multi-agent systems introduce no uncertainties into the ANI pipeline. This is true even for poorly behaving UWB-clocks.

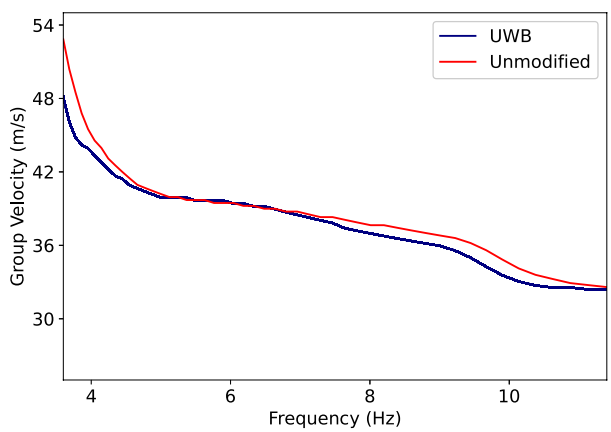

Figure 8. 1,000 overlapping dispersion curves from ultra-wideband clock simulations on G3 and G4 with $\omega_0 = 8$ and unmodified dispersion curve.

7.3. CWT-Induced Time-Lag Uncertainty

Now, we consider the uncertainties in the velocity estimates arising solely from the CWT and the corresponding Heisenberg-Gabor uncertainty principle. The results are shown in Figure 9. As expected, with lower frequency (i.e., larger scale s), the time uncertainty increases (Equation 9) and therefore the uncertainty in the velocity estimates. The choice of ω_0 also influences the magnitude of uncertainty, with lower values of ω_0 resulting in smaller uncertainties in time. There is a trade-off however, as the energy-spread in the frequency domain increases with lower time uncertainty. This might explain the more flat shape of the $\omega_0 = 4$-dispersion curve: as energy is smeared over multiple frequencies, it becomes more difficult to discern between different time lags of affected frequencies (Figure 6).

There is a substantial uncertainty involved in picking the maximum energy, that is, time lag, due to the CWT's joint-resolution limit. We therefore investigate how the theoretical energy spread in time due to Heisenberg-Gabor

23335084, 2026, 2, Downloaded from https://agupubs.onlinelibrary.wiley.com/doi/10.1029/2025EA004631 by Dtsch Zentrum F. Luft-U. Raum Fahrt In D. Helmholtz Gemein., Wiley Online Library on [24/02/2026]. See the Terms and Conditions (https://onlinelibrary.wiley.com/terms-and-conditions) on Wiley Online Library for rules of use; OA articles are governed by the applicable Creative Commons License

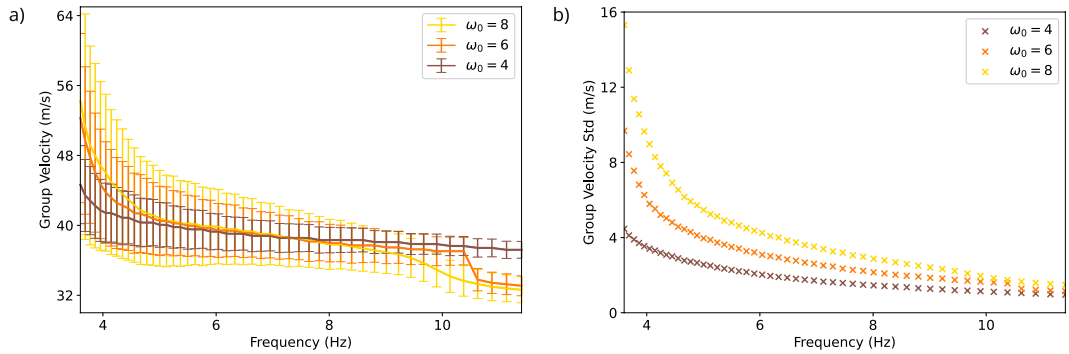

Figure 9. Dispersion curves for different ω_0s with standard deviation of the velocity estimates solely due to the Heisenberg-Gabor uncertainty (a) and closer look at the standard deviations (b).

uncertainty compares to the scalogram around the picked time lags. We do this only for $\omega_0 = 6$ by cutting out the Green's function from the scalogram. Figure 10 exemplary shows the behavior throughout, where for lower frequencies the theoretical energy spread is smaller than the one observed, whereas it matches very well for higher energy areas in the scalogram (5 Hz to 8 Hz). For even higher frequencies, the main peak of the Green's function is also well-matched, with close-by side-peaks of lower amplitude appearing. These could stem from a less clear retrieval of the Green's function due to a worse SNR in combination with a decrease in Heisenberg-Gabor uncertainty in time. The small mismatch for the lower frequencies could also stem from a less clear retrieval of the Green's function due to lower SNR or energy contributions from slightly larger traveltimes. These findings demonstrate that the observed energy spread in the scalogram closely matches the normal distribution $\mathcal{N}(\mu_{E,t}, \sigma_{E,t})$ predicted by the Heisenberg-Gabor uncertainty principle.

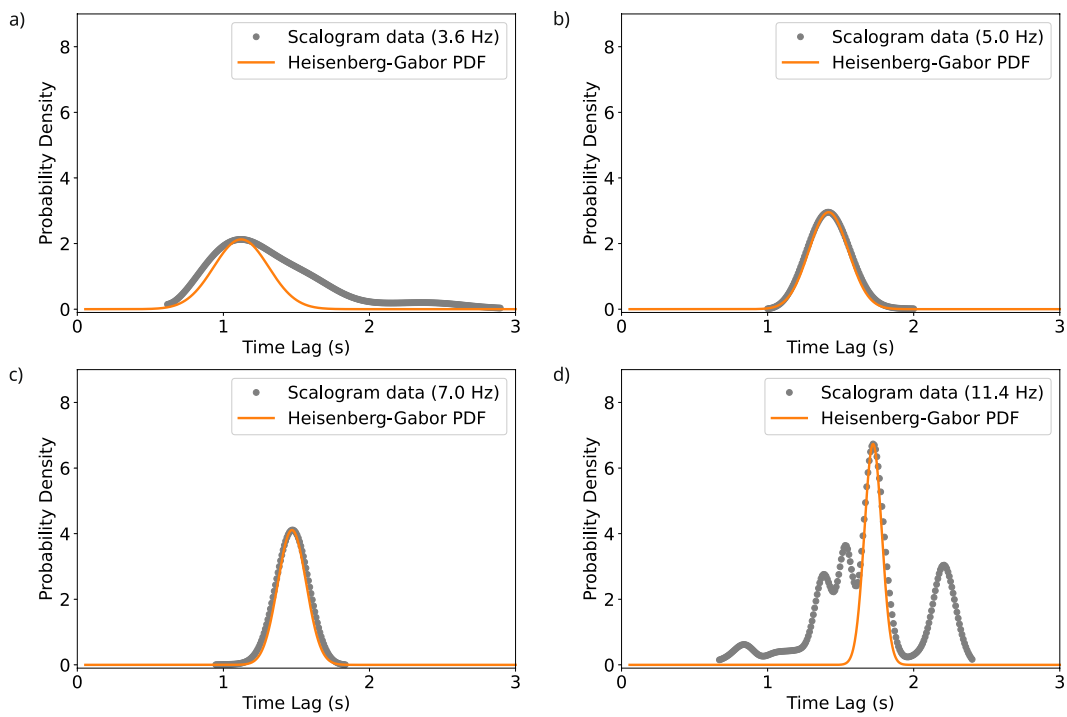

Figure 10. Normal distributions derived from Heisenberg-Gabor uncertainty centered on time-lag pick compared to amplitude-scaled values in the scalogram; derived with $\omega_0 = 6$ for frequencies (a) 3.6 Hz, (b) 5.0 Hz, (c) 7.0 Hz, and (d) 11.4 Hz.

23335084, 2026, 2, Downloaded from https://agupubs.onlinelibrary.wiley.com/doi/10.1029/2025EA004631 by Dtsch Zentrum F. Luft-U. Raum Fahrt In D. Helmholtz Gemein., Wiley Online Library on [24/02/2026]. See the Terms and Conditions (https://onlinelibrary.wiley.com/terms-and-conditions) on Wiley Online Library for rules of use; OA articles are governed by the applicable Creative Commons License

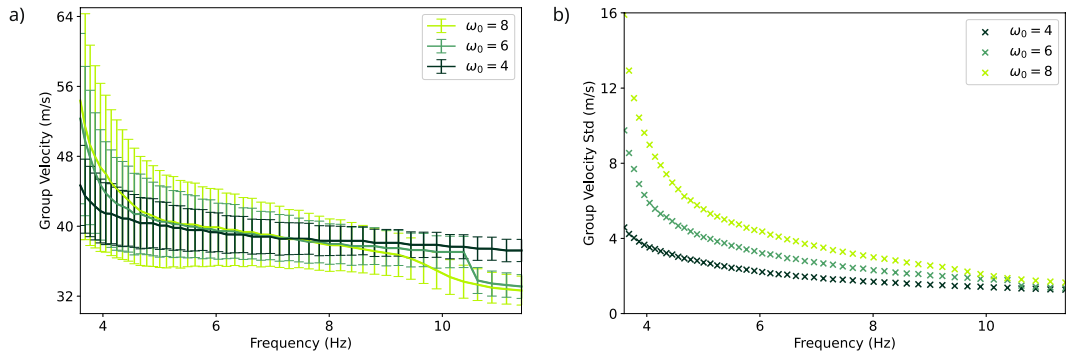

Figure 11. Dispersion curves for different ω_0s with standard deviation of the velocity estimates due to the combination of localization and Heisenberg-Gabor uncertainty (a) and closer look at the standard deviations (b).

7.4. Combined Uncertainties

Finally, we combine the localization uncertainty and the uncertainty in time-lag estimation. The dispersion curves and standard deviations of the velocity estimates shown in Figure 11 are very similar to the ones that are purely due to time-lag uncertainty (Figure 9). The histograms of the velocity samples for $\omega_0 = 6$ in Figure 12 confirm the observation that the combination of these factors leads to a very similar result as if only the time-lag induced velocity uncertainties are accounted for. The distribution of the velocity samples are right skewed for the localization and combined uncertainty cases, which is especially noticeable for smaller frequencies. This is due to the truncated normal distributions of the time lags having their mean closer to zero for faster seismic velocities.

The calculated covariance between samples of L and T^{-1} is $\mathrm{Cov}\left[L, T^{-1}\right] = -2.4 \cdot 10^{-4}$. This minor covariance results in a relative error incurred by dropping the covariance term in the Taylor approximation of $\mathrm{Var}[V]$ (Equation 16) of 0.62 %. This indicates that we can assume independence of L and T^{-1}. We further justify the usage of Equation 15 by calculating the difference to the Taylor approximation of $\mathrm{Var}[V]$. A relative error of 0.04 % confirms our choice of using Equation 15 with its assumption on independence.

7.5. Analytical Versus Simulation-Derived Moments

In this last step, we validate our analytical derivations. First, the comparison between analytical and simulated means and standard deviations for the most complex case of combined uncertainties in localization and time-lag picking is presented in Figure 13. Both the mean and standard deviation show only minor differences (<1 %), except at the lowest frequencies for $\omega_0 = 8$. In these cases, the relatively large standard deviation combined with the smaller mean traveltimes leads to violation of Inequality (11), reducing the accuracy of the approximated inverse moments at these frequencies.

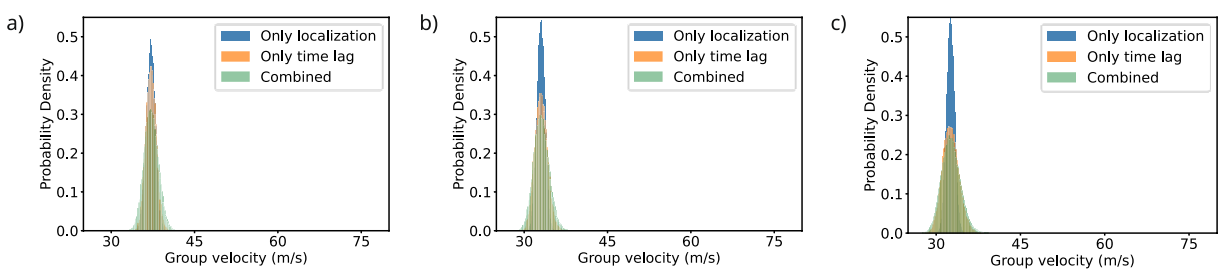

Figure 12. Histogram of velocity samples at (a) 3.6 Hz, (b) 7.0 Hz, and (c) 11.4 Hz for the three simulations: accounting only for localization uncertainty, only for CWT-induced time-lag uncertainty and the combination of the two.

23335084, 2026, 2, Downloaded from https://agupubs.onlinelibrary.wiley.com/doi/10.1029/2025EA004631 by Dtsch Zentrum F. Luft-U. Raum Fahrt In D. Helmholtz Gemein., Wiley Online Library on [24/02/2026]. See the Terms and Conditions (https://onlinelibrary.wiley.com/terms-and-conditions) on Wiley Online Library for rules of use; OA articles are governed by the applicable Creative Commons License

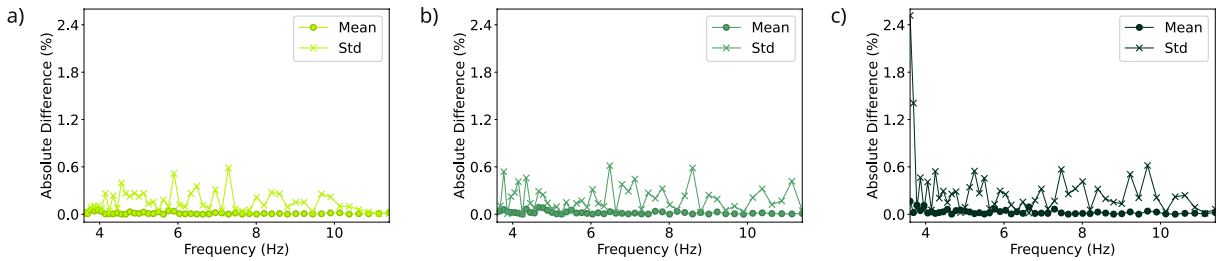

Figure 13. Difference between sampled and analytically calculated moments of the velocity estimates due to combined uncertainties for (a) $\omega_0 = 4$, (b) $\omega_0 = 6$, and (c) $\omega_0 = 8$.

Since the simulated moments closely match the analytical ones, we conclude that our derivation for the velocity distribution moments is sound. However, as the approximation for the inverse moments depends on Inequality (11), some combinations of receiver distance and seismic velocities that could appear in lunar experiments may not meet this criterion, resulting in larger approximation errors. Addressing this limitation would require either a different approach to the approximation or explicitly accounting for these errors.

8. Conclusion and Future Work

In this work, we conducted an end-to-end assessment of uncertainties associated with multi-agent lunar seismic ambient noise exploration, particularly focusing on the impact of localization errors, clock instabilities, and the limitations of the CWT. Our comprehensive approach to account for both measurement and processing errors leads to these main finding:

1. Localization uncertainties for realistic agent position standard deviations of 0.9 m translate into velocity standard deviations below <1.2 m/s for Rayleigh-wave velocities up to 54 m/s at a receiver distance of 56.9 m. This accuracy level is sufficient for most kind of experiments, for example, to discriminate between regolith with near-surface ice versus regolith without (Keil, Schimmel, & Igel, 2025, Figure 7).
2. Clock instabilities are negligible for lunar ANI, even in case of poorly performing UWB clocks with periodic, but perfect synchronization. However, additional tests are required to validate these findings for more realistic lunar conditions, for example for potentially thermal-induced variations in clock stability and non-perfect synchronization algorithms.
3. CWT-induced uncertainties arising from the Heisenberg-Gabor uncertainty principle dominate the overall velocity uncertainties. The choice of wavelet parameter ω_0 is crucial in determining a balance between temporal and frequency resolution.
4. Our derived analytical error model accurately reproduces the results of the simulations. This provides an efficient method to predict uncertainties, allowing for the optimization of seismic network configurations and processing parameters.

Understanding and quantifying these uncertainties is crucial for two primary reasons. First, reliably detecting lunar subsurface structures such as ice deposits or lava tubes requires clear differentiation between dispersion curves from disturbed and undisturbed media. Quantifying uncertainties ensures that identified velocity variations represent genuine subsurface features rather than measurement artifacts. Currently, parameter studies and simulations targeting lunar ice and lava tubes are ongoing (Keil, Schimmel, & Igel, 2025; Keil, Sesko, et al., 2025). Second, the derived analytical framework enables direct optimization of multi-agent network strategies. Specifically, we could now adjust receiver spacing and wavelet parameters (ω_0) to minimize velocity uncertainties to acceptable levels.

To advance this research further, several directions are particularly promising. First, enhance the data processing method to remove the uncertainty bottleneck in the CWT by for example, exploring super-resolution techniques

23335084, 2026, 2, Downloaded from https://agupubs.onlinelibrary.wiley.com/doi/10.1029/2025EA004631 by Dtsch Zentrum F. Luft-U. Raum Fahrt In D. Helmholtz Gemein., Wiley Online Library on [24/02/2026]. See the Terms and Conditions (https://onlinelibrary.wiley.com/terms-and-conditions) on Wiley Online Library for rules of use; OA articles are governed by the applicable Creative Commons License

(Moca et al., 2021) or adaptive wavelet dictionaries using a matching pursuit algorithm (Mallat, 2009). Second, extending our framework to full multi-station arrays with CRB-inspired position errors. Third, we aim to develop optimal exploration strategies that integrate the uncertainties addressed in this study with additional sources of uncertainty, such as those induced by terrain and subsurface heterogeneity, within a seismic optimal-experimental-design framework.

Appendix A: Continuous Wavelet Transform

The CWT employes a normalized mother wavelet ψ with zero mean

$$\int_{-\infty}^{\infty} \psi(t)\, dt = 0\,, \qquad \|\psi\| = \sqrt{\int_{-\infty}^{\infty} \psi(t)^2\, dt} = 1 \tag{A1}$$

that satisfies the admissibility criterion

$$C_\psi = \int_0^{\infty} \frac{|\hat{\psi}(\omega)|^2}{\omega}\, d\omega \;<\; \infty. \tag{A2}$$

Here, $\hat{\psi}(\omega)$ denotes the Fourier transform of $\psi(t)$. The (Equation A2) criterion guarantees completeness and energy conservation of the transform. The wavelet is dilated with scale parameter $s > 0$ (inversely proportional to frequency) and translated by $u \in \mathbb{R}$ to create a wavelet dictionary

$$\mathcal{D} = \left\{ \psi_{u,s}(t) = \frac{1}{\sqrt{s}} \psi\left(\frac{t-u}{s}\right) \right\}. \tag{A3}$$

The CWT of a signal $f(t)$ is then defined by

$$W_f(u,s) \;=\; \langle f, \psi_{u,s} \rangle \;=\; \int_{-\infty}^{\infty} f(t) \psi^*_{u,s}(t)\, dt, \tag{A4}$$

with $\psi^*_{u,s}(t)$ the complex conjugate of $\psi_{u,s}(t)$.

The scalogram is defined as the squared modulus of wavelet coefficients $|W_f(u,s)|^2$. Typically, these are calculated as in Equation A4, representing a L^2-norm (Torrence & Compo, 1998). It should be noted that it is also possible to use the L^1-norm by using $1/s$ as a coefficient for $\psi_{u,s}(t)$, which preserves amplitude with scale, but not energy (Liu et al., 2007). In numerical applications, energy is inherently lost, making it a viable choice (The MathWorks Inc, 2024). Because part of our treatment is analytic, we utilize the definition based on the L^2-norm.

The joint time-frequency resolution of the CWT is limited due to the Heisenberg-Gabor uncertainty principle

$$\sigma_t \sigma_\omega \geq \frac{1}{2}, \tag{A5}$$

where, for a unit-energy wavelet,

$$\sigma_t^2 = \int_{-\infty}^{\infty} t^2 |\psi(t)|^2\, dt \qquad \text{and} \qquad \sigma_\omega^2 = \int_{-\infty}^{\infty} \omega^2 |\hat{\psi}(\omega)|^2\, d\omega. \tag{A6}$$

The Morlet wavelet used in our study has a time variance of

23335084, 2026, 2, Downloaded from https://agupubs.onlinelibrary.wiley.com/doi/10.1029/2025EA004631 by Dtsch Zentrum F. Luft-U. Raum Fahrt In D. Helmholtz Gemein., Wiley Online Library on [24/02/2026]. See the Terms and Conditions (https://onlinelibrary.wiley.com/terms-and-conditions) on Wiley Online Library for rules of use; OA articles are governed by the applicable Creative Commons License

$$
\begin{aligned}
\sigma_t^2 &= \int_{-\infty}^{+\infty} t^2 \left| \pi^{-1/4} e^{i\omega_0 t} e^{-t^2/2} \right|^2 dt \\
&= \pi^{-1/2} \int_{-\infty}^{+\infty} t^2 \left| e^{-t^2/2} \left[\cos(\omega_0 t) + i \sin(\omega_0 t) \right] \right|^2 dt \\
&= \pi^{-1/2} \int_{-\infty}^{+\infty} t^2 \left(e^{-t^2/2} \right)^2 dt \\
&= 2\pi^{-1/2} \int_{0}^{+\infty} t^2 e^{-t^2} dt \\
&\quad \text{Let } u = t^2 \Rightarrow t = \sqrt{u},\ dt = \frac{du}{2\sqrt{u}} \\
&= \pi^{-1/2} \int_{0}^{+\infty} \frac{u}{u^{1/2}} e^{-u} du \\
&= \pi^{-1/2} \int_{0}^{+\infty} u^{1/2} e^{-u} du \\
&= \pi^{-1/2} \Gamma\left(\frac{3}{2}\right) \\
&= \frac{1}{2}
\end{aligned}
\tag{A7}
$$

and therefore a temporal energy spread of

$$
\sigma_{E,t} := \sqrt{\sigma_t^2} = \frac{1}{\sqrt{2}}. \tag{A8}
$$

We omit the explicit derivation of the corresponding frequency variance $\sigma_\omega^2 = 1/2$, as our focus is on the temporal uncertainties.

Conflict of Interest

The authors declare no conflicts of interest relevant to this study.

Data Availability Statement

The analyzed passive Apollo 17 data were downloaded from the Data ARchives and Transmission System (DARTS) (DARTS, 2020). The code used for this study can be found at https://github.com/DLR-KN/LunarANI-UQ (Nierula & Keil, 2025).

Acknowledgments
This work is supported by the NEPOS project (Project number: 517291159), funded by the Deutsche Forschungsgemeinschaft (DFG, German Research Foundation). Open Access funding enabled and organized by Projekt DEAL.

References

Allan, D. (1966). Statistics of atomic frequency standards. *Proceedings of the IEEE*, *54*(2), 221–230. https://doi.org/10.1109/PROC.1966.4634

Ash, J. N., & Moses, R. L. (2008). On the relative and absolute positioning errors in self-localization systems. *IEEE Transactions on Signal Processing*, *56*(11), 5668–5679. https://doi.org/10.1109/TSP.2008.927072

Benna, M., Schmerr, N., Sarantos, M., Bailey, H., Gershman, D., Horanyi, M., et al. (2020). The lunar environment monitoring station (LEMS). In *Europlanet science congress 2020*. https://doi.org/10.5194/epsc2020-60

Bensen, G. D., Ritzwoller, M. H., Barmin, M. P., Levshin, A. L., Lin, F., Moschetti, M. P., et al. (2007). Processing seismic ambient noise data to obtain reliable broad-band surface wave dispersion measurements. *Geophysical Journal International*, *169*(3), 1239–1260. https://doi.org/10.1111/j.1365-246X.2007.03374.x

Blanchette-Guertin, J.-F., Johnson, C. L., & Lawrence, J. F. (2015). Modeling seismic energy propagation in highly scattering environments. *Journal of Geophysical Research: Planets*, *120*(3), 515–537. https://doi.org/10.1002/2014JE004654

Brambilla, M., Ferrante, E., Birattari, M., & Dorigo, M. (2013). Swarm robotics: A review from the swarm engineering perspective. *Swarm Intelligence*, *7*(1), 1–41. https://doi.org/10.1007/s11721-012-0075-2

Carrer, L., Pozzobon, R., Sauro, F., Castelletti, D., Patterson, G. W., & Bruzzone, L. (2024). Radar evidence of an accessible cave conduit on the Moon below the Mare Tranquillitatis pit. *Nature Astronomy*, *8*(9), 1–8. https://doi.org/10.1038/s41550-024-02302-y

Chang, C., & Sahai, A. (2006). Cramér-Rao-Type bounds for localization. *EURASIP Journal on Applied Signal Processing*, *2006*(1), 1–13. https://doi.org/10.1155/ASP/2006/94287

23335084, 2026, 2, Downloaded from https://agupubs.onlinelibrary.wiley.com/doi/10.1029/2025EA004631 by Dtsch Zentrum F. Luft-U. Raum Fahrt In D. Helmholtz Gemein., Wiley Online Library on [24/02/2026]. See the Terms and Conditions (https://onlinelibrary.wiley.com/terms-and-conditions) on Wiley Online Library for rules of use; OA articles are governed by the applicable Creative Commons License

Chappaz, L., Sood, R., Melosh, H. J., Howell, K. C., Blair, D. M., Milbury, C., & Zuber, M. T. (2017). Evidence of large empty lava tubes on the Moon using GRAIL gravity. *Geophysical Research Letters*, *44*(1), 105–112. https://doi.org/10.1002/2016GL071588

Cohen, L. (2001). The uncertainty principle for the short-time fourier transform and wavelet transform. In L. Debnath (Ed.), *Wavelet transforms and time-frequency signal analysis* (pp. 217–232). Birkhäuser. https://doi.org/10.1007/978-1-4612-0137-3_8

Conti, A., Guerra, M., Dardari, D., Decarli, N., & Win, M. Z. (2012). Network experimentation for cooperative localization. *IEEE Journal on Selected Areas in Communications*, *30*(2), 467–475. https://doi.org/10.1109/JSAC.2012.120227

Cooper, M. R., Kovach, R. L., & Watkins, J. S. (1974). Lunar near-surface structure. *Reviews of Geophysics*, *12*(3), 291–308. https://doi.org/10.1029/RG012i003p00291

Cramér, H. (1946). *Mathematical methods of statistics*. Princeton University Press.

Dainty, A. M., Toksöz, M. N., Anderson, K. R., Pines, P. J., Nakamura, Y., & Latham, G. (1974). Seismic scattering and shallow structure of the moon in oceanus procellarum. *The Moon*, *9*(1), 11–29. https://doi.org/10.1007/BF00565388

DARTS. (2020). Apollo passive seismic observation data [Dataset]. Retrieved from https://darts.isas.jaxa.jp/en/datasets/darts:apollo-pse-data

de la Croix, J.-P., Rossi, F., Brockers, R., Aguilar, D., Albee, K., Boroson, E., et al. (2024). Multi-agent autonomy for space exploration on the CADRE lunar technology demonstration. In *2024 IEEE aerospace conference* (pp. 1–14). https://doi.org/10.1109/AERO58975.2024.10521425

Duennebier, F., & Sutton, G. H. (1974). Thermal moonquakes. *Journal of Geophysical Research (1896-1977)*, *79*(29), 4351–4363. https://doi.org/10.1029/JB079i029p04351

Galleani, L., Sacerdote, L., Tavella, P., & Zucca, C. (2003). A mathematical model for the atomic clock error. *Metrologia*, *40*(3), S257–S264. https://doi.org/10.1088/0026-1394/40/3/305

Goodman, L. A. (1960). On the exact variance of products. *Journal of the American Statistical Association*, *55*(292), 708–713. https://doi.org/10.1080/01621459.1960.10483369

Gupta, P., & Mukhopadhyay, S. (2023). Extraction of group velocity dispersion curves of surface waves using continuous wavelet transform. *IEEE Geoscience and Remote Sensing Letters*, *20*, 1–5. https://doi.org/10.1109/LGRS.2023.3287470

Haase, I., Wählisch, M., Gläser, P., Oberst, J., & Robinson, M. S. (2019). Coordinates and maps of the apollo 17 landing site. *Earth and Space Science*, *6*(1), 59–95. https://doi.org/10.1029/2018EA000408

Hall, R. L. (1979). Inverse moments for a class of truncated normal distributions. *Sankhyā: The Indian Journal of Statistics, Series B (1960-2002)*, *41*(1/2), 66–76.

Haruyama, J., Morota, T., Kobayashi, S., Sawai, S., Lucey, P. G., Shirao, M., & Nishino, M. N. (2012). Lunar holes and lava tubes as resources for lunar science and exploration. In V. Badescu (Ed.), *Moon: Prospective energy and material resources* (pp. 139–163). Springer. https://doi.org/10.1007/978-3-642-27969-0_6

Haviland, H. F., Weber, R. C., Neal, C. R., Lognonné, P., Garcia, R. F., Schmerr, N., et al. (2022). The lunar geophysical network landing sites science rationale. *The Planetary Science Journal*, *3*(2), 40. https://doi.org/10.3847/PSJ/ac0f82

Holschneider, M., Diallo, M. S., Kulesh, M., Ohrnberger, M., Lück, E., & Scherbaum, F. (2005). Characterization of dispersive surface waves using continuous wavelet transforms. *Geophysical Journal International*, *163*(2), 463–478. https://doi.org/10.1111/j.1365-246X.2005.02787.x

Horz, F. (1985). Lava tubes - Potential shelters for habitats. In W. W. Mendell (Ed.), *Lunar bases and space activities of the 21st century* (pp. 405–412).

Keil, S., Igel, H., Schimmel, M., Lindner, F., & Bernauer, F. (2024). Investigating subsurface properties of the shallow lunar crust using seismic interferometry on synthetic and recorded data. *Earth and Space Science*, *11*(10), e2024EA003742. https://doi.org/10.1029/2024EA003742

Keil, S., Schimmel, M., & Igel, H. (2025). Evaluating seismic ambient noise techniques for detecting ice-bearing rocks on the moon. *Earth and Space Science*, *12*(9), e2025EA004369. https://doi.org/10.1029/2025EA004369

Keil, S., Sesko, R., Schimmel, M., Igel, H., & Reiss, P. (2025). Evaluating seismic ambient noise techniques for imaging lava tubes on the moon. *ESS Open Archive*. https://doi.org/10.22541/essoar.176522199.94119499/v1

Kolesnikov, Y. I., & Fedin, K. (2018). Detecting underground cavities using microtremor data: Physical modelling and field experiment. *Geophysical Prospecting*, *66*(2), 342–353. https://doi.org/10.1111/1365-2478.12540

Kovach, R. L., Watkins, S., & Talwani, P. (1973). *Lunar seismic profiling experiment (Apollo 17: Preliminary science report No. 330)*. NASA Special Publication. Retrieved from https://ntrs.nasa.gov/citations/19740010327

Kulesh, M., Holschneider, M., Diallo, M. S., Xie, Q., & Scherbaum, F. (2005). Modeling of wave dispersion using continuous wavelet transforms. *Pure and Applied Geophysics*, *162*(5), 843–855. https://doi.org/10.1007/s00024-004-2644-9

Kulesh, M., Holschneider, M., Ohrnberger, M., & Lück, E. (2008). Modeling of wave dispersion using continuous wavelet transforms II: Wavelet-based frequency-velocity analysis. *Pure and Applied Geophysics*, *165*(2), 255–270. https://doi.org/10.1007/s00024-008-0299-7

Kunimasu, T., Sawayama, K., & Tsuji, T. (2023). Estimation of the mass fraction and distribution of ice in a lunar regolith simulant from seismic velocity. *Icarus*, *406*, 115725. https://doi.org/10.1016/j.icarus.2023.115725

Larose, E., Khan, A., Nakamura, Y., & Campillo, M. (2005). Lunar subsurface investigated from correlation of seismic noise. *Geophysical Research Letters*, *32*(16). https://doi.org/10.1029/2005GL023518

Lecocq, T., Caudron, C., & Brenguier, F. (2014). MSNoise, a python package for monitoring seismic velocity changes using ambient seismic noise. *Seismological Research Letters*, *85*(3), 715–726. https://doi.org/10.1785/0220130073

Levine, J. (1999). Introduction to time and frequency metrology. *Review of Scientific Instruments*, *70*(6), 2567–2596. https://doi.org/10.1063/1.1149844

Lin, F.-C., Ritzwoller, M. H., Townend, J., Bannister, S., & Savage, M. K. (2007). Ambient noise Rayleigh wave tomography of New Zealand. *Geophysical Journal International*, *170*(2), 649–666. https://doi.org/10.1111/j.1365-246X.2007.03414.x

Liu, L., Hsu, H., & Grafarend, E. W. (2007). Normal Morlet wavelet transform and its application to the Earth's polar motion. *Journal of Geophysical Research*, *112*(B8). https://doi.org/10.1029/2006JB004895

Lobkis, O. I., & Weaver, R. L. (2001). On the emergence of the Green's function in the correlations of a diffuse field. *Journal of the Acoustical Society of America*, *110*(6), 3011–3017. https://doi.org/10.1121/1.1417528

Ma, L., Han, L., Feng, Q., & Li, X. (2024). Real-time passive seismic interferometry with deep transfer learning. *IEEE Transactions on Geoscience and Remote Sensing*, *62*, 1–9. https://doi.org/10.1109/TGRS.2024.3365688

Mallat, S. (2009). *A wavelet tour of signal processing* (3rd ed.). Academic Press.

McClanahan, T. P., Parsons, A. M., Livengood, T. A., Su, J. J., Chin, G., Hamara, D., et al. (2024). Evidence for widespread hydrogen sequestration within the moon's south pole cold traps. *The Planetary Science Journal*, *5*(10), 217. https://doi.org/10.3847/PSJ/ad5b55

Moca, V. V., Bârzan, H., Nagy-Dăbâcan, A., & Murean, R. C. (2021). Time-frequency super-resolution with superlets. *Nature Communications*, *12*(1), 337. https://doi.org/10.1038/s41467-020-20539-9

23335084, 2026, 2, Downloaded from https://agupubs.onlinelibrary.wiley.com/doi/10.1029/2025EA004631 by Dtsch Zentrum F. Luft-U. Raum Fahrt In D. Helmholtz Gemein., Wiley Online Library on [24/02/2026]. See the Terms and Conditions (https://onlinelibrary.wiley.com/terms-and-conditions) on Wiley Online Library for rules of use; OA articles are governed by the applicable Creative Commons License

Nierula, K., & Keil, S. (2025). Code for evaluating multi-agent and wavelet-transform uncertainties in lunar seismic ambient noise exploration [Software]. *Deutsches Zentrum für Luft- und Raumfahrt e. V. (DLR)*. https://doi.org/10.26090/CKHM-HN79

Panning, M., Kedar, S., Bowles, N., Calcutt, S., Drilleau, M., Garcia, R., et al. (2022). Farside seismic suite (FSS): First-ever seismology on the farside of the moon and a model for long-lived lunar science. In *Europlanet science congress 2022* (pp. EPSC2022–EPSC2672). Granada. https://doi.org/10.5194/epsc2022-672

Poggi, V., Fäh, D., & Giardini, D. (2013). Time–frequency–wavenumber analysis of surface waves using the continuous wavelet transform. *Pure and Applied Geophysics*, *170*(3), 319–335. https://doi.org/10.1007/s00024-012-0505-5

Pöhlmann, R., Staudinger, E., Zhang, S., Broghammer, F., Dammann, A., & Hoeher, P. A. (2023). Cooperative radio navigation for robotic exploration: Evaluation of a space-analogue mission. In *2023 IEEE/ION position, location and navigation symposium (PLANS)* (pp. 372–380). https://doi.org/10.1109/PLANS53410.2023.10140026

Rao, C. R. (1992). Information and the accuracy attainable in the estimation of statistical parameters. In S. Kotz & N. L. Johnson (Eds.), *Breakthroughs in statistics: Foundations and basic theory* (pp. 235–247). Springer. https://doi.org/10.1007/978-1-4612-0919-5_16

Reach, W. T., Lucey, P. G., Honniball, C. I., Arredondo, A., & Malaret, E. R. (2023). The distribution of molecular water in the lunar south polar region based upon 6 μm spectroscopic imaging. *The Planetary Science Journal*, *4*(3), 45. https://doi.org/10.3847/PSJ/acbdf2

Rice, S. O. (1945). Mathematical analysis of random noise. *Bell System Technical Journal*, *24*(1), 46–156. https://doi.org/10.1002/j.1538-7305.1945.tb00453.x

Saboia, M., Rossi, F., Nguyen, V., Lim, G., & Aguilar, D. (2024). CADRE MoonDB: Distributed database for multi-robot information-sharing and map-merging for lunar exploration. In *Proceedings of the 23rd international conference on autonomous agents and multiagent systems*.

Sabra, K. G., Gerstoft, P., Roux, P., Kuperman, W. A., & Fehler, M. C. (2005). Extracting time-domain Green's function estimates from ambient seismic noise. *Geophysical Research Letters*, *32*(3). https://doi.org/10.1029/2004GL021862

Şahin, E. (2005). Swarm robotics: From sources of inspiration to domains of application. In E. Şahin & W. M. Spears (Eds.), *Swarm robotics* (pp. 10–20). https://doi.org/10.1007/978-3-540-30552-1_2

Savic, V., & Zazo, S. (2018). Belief propagation techniques for cooperative localization in wireless sensor networks. In *Handbook of position location* (pp. 967–998). Wiley. https://doi.org/10.1002/9781119434610.ch26

Schuster, M. J., Müller, M. G., Brunner, S. G., Lehner, H., Lehner, P., Sakagami, R., et al. (2020). The ARCHES space-analogue demonstration mission: Towards heterogeneous teams of autonomous robots for collaborative scientific sampling in planetary exploration. *IEEE Robotics and Automation Letters*, *5*(4), 5315–5322. https://doi.org/10.1109/LRA.2020.3007468

Sens-Schönfelder, C., & Larose, E. (2010). Lunar noise correlation, imaging and monitoring. *Earthquake Science*, *23*(5), 519–530. https://doi.org/10.1007/s11589-010-0750-6

Shapiro, N. M., & Campillo, M. (2004). Emergence of broadband rayleigh waves from correlations of the ambient seismic noise. *Geophysical Research Letters*, *31*(7). https://doi.org/10.1029/2004GL019491

Shen, Y., & Win, M. Z. (2010). Fundamental limits of wideband localization—Part I: A general framework. *IEEE Transactions on Information Theory*, *56*(10), 4956–4980. https://doi.org/10.1109/TIT.2010.2060110

Sichitiu, M., & Veerarittiphan, C. (2003). Simple, accurate time synchronization for wireless sensor networks. In *2003 IEEE wireless communications and networking, 2003. WCNC 2003* (Vol. 2, pp. 1266–1273). https://doi.org/10.1109/WCNC.2003.1200555

Spudis, P. D. (1999). The case for renewed human exploration of the moon. *Earth, Moon, and Planets*, *87*(3), 159–171. https://doi.org/10.1023/A:1013186823933

Staudinger, E., Giubilato, R., Schuster, M. J., Pöhlmann, R., Zhang, S., Dömel, A., et al. (2023). Terrain-aware communication coverage prediction for cooperative networked robots in unstructured environments. *Acta Astronautica*, *202*, 799–805. https://doi.org/10.1016/j.actaastro.2022.10.050

Staudinger, E., Zhang, S., Pöhlmann, R., & Dammann, A. (2021). The role of time in a robotic swarm: A joint view on communications, localization, and sensing. *IEEE Communications Magazine*, *59*(2), 98–104. https://doi.org/10.1109/MCOM.001.2000593

Strutz, D., & Curtis, A. (2024). Variational Bayesian experimental design for geophysical applications: Seismic source location, amplitude versus offset inversion, and estimating CO2 saturations in a subsurface reservoir. *Geophysical Journal International*, *236*(3), 1309–1331. https://doi.org/10.1093/gji/ggad492

Stuart, A., & Ord, J. K. (1994). *Kendall's advanced theory of statistics, distribution theory* (6th ed.). Wiley.

Talwani, M., & Kessinger, W. (2003). Exploration geophysics. In R. A. Meyers (Ed.), *Encyclopedia of physical science and technology* (3rd ed., pp. 709–726). Academic Press. https://doi.org/10.1016/B0-12-227410-5/00238-6

Tanimoto, T., Eitzel, M., & Yano, T. (2008). The noise cross-correlation approach for Apollo 17 LSPE data: Diurnal change in seismic parameters in shallow lunar crust. *Journal of Geophysical Research*, *113*(E8). https://doi.org/10.1029/2007JE003016

The MathWorks Inc. (2024). cwt. Retrieved from https://de.mathworks.com/help/wavelet/ref/cwt.html

Torrence, C., & Compo, G. P. (1998). A practical guide to wavelet analysis. *Bulletin of the American Meteorological Society*, *79*(1), 61–78. https://doi.org/10.1175/1520-0477(1998)079⟨0061:APGTWA⟩2.0.CO;2

Trainotti, C., Schmidt, T., & Furthner, J. (2019). Comparison of clock models in view of clock composition, clock steering and measurement fitting. In *50th annual precise time and time interval systems and applications meeting* (pp. 265–283). https://doi.org/10.33012/2019.16756

Williams, J. P., Paige, D. A., Greenhagen, B. T., & Sefton-Nash, E. (2017). The global surface temperatures of the Moon as measured by the Diviner lunar radiometer experiment. *Icarus*, *283*, 300–325. https://doi.org/10.1016/j.icarus.2016.08.012

Wymeersch, H., Lien, J., & Win, M. Z. (2009). Cooperative localization in wireless networks. *Proceedings of the IEEE*, *97*(2), 427–450. https://doi.org/10.1109/JPROC.2008.2008853

Yang, Y., Ritzwoller, M. H., Levshin, A. L., & Shapiro, N. M. (2007). Ambient noise Rayleigh wave tomography across Europe. *Geophysical Journal International*, *168*(1), 259–274. https://doi.org/10.1111/j.1365-246X.2006.03203.x

Zhang, S., Pöhlmann, R., Staudinger, E., & Dammann, A. (2021). Assembling a swarm navigation system: Communication, localization, sensing and control. In *2021 IEEE 18th annual consumer communications and networking conference (CCNC)* (pp. 1–9). https://doi.org/10.1109/CCNC49032.2021.9369547

Zhang, S., Ruz, P. F., Broghammer, F., Staudinger, E., Gentner, C., Pöhlmann, R., et al. (2023). Self-organized UWB localization for robotic swarm – First results from an analogue mission on volcano etna. In *2023 IEEE aerospace conference* (pp. 1–11). https://doi.org/10.1109/AERO55745.2023.10115558

23335084, 2026, 2, Downloaded from https://agupubs.onlinelibrary.wiley.com/doi/10.1029/2025EA004631 by Dtsch Zentrum F. Luft-U. Raum Fahrt In D. Helmholtz Gemein., Wiley Online Library on [24/02/2026]. See the Terms and Conditions (https://onlinelibrary.wiley.com/terms-and-conditions) on Wiley Online Library for rules of use; OA articles are governed by the applicable Creative Commons License